

# Three-Dimensional In-Situ Imaging of Single-Grain Growth in Polycrystalline Films

Dmitry Dzhigaev (✉ [dmitry.dzhigaev@sljus.lu.se](mailto:dmitry.dzhigaev@sljus.lu.se))

Lund University

Pierre-Alexis Repecaud

University of Twente

Yury Smirnov

University of Twente

Lucas Marçal

Lund Univrsity <https://orcid.org/0000-0003-4956-5144>

Giovanni Fevola

Deutsches Elektronen-Synchrotron DESY

Dina Sheyfer

Deutsche Elektronen-Synchrotron DESY

Quentin Jeangros

École Polytechnique Fédérale de Lausanne <https://orcid.org/0000-0003-2885-975X>

Wonsuk Cha

Argonne National Laboratory <https://orcid.org/0000-0001-8888-4258>

Ross Harder

Argonne National Laboratory

Anders Mikkelsen

Lund University

Jesper Wallentin

Lund University <https://orcid.org/0000-0001-5909-0483>

Monica Morales-Masis

University of Twente

Michael Stuckelberger

Deutsches Elektronen-Synchrotron DESY <https://orcid.org/0000-0002-8244-5235>

---

## Article

### Keywords:

**Posted Date:** February 15th, 2022

DOI: <https://doi.org/10.21203/rs.3.rs-1228565/v1>

**License:**  This work is licensed under a Creative Commons Attribution 4.0 International License.

[Read Full License](#)

---

**Version of Record:** A version of this preprint was published at Communications Materials on June 17th, 2022. See the published version at <https://doi.org/10.1038/s43246-022-00260-4>.

# Three-dimensional in-situ imaging of single-grain growth in polycrystalline films

Dmitry Dzhigaev,<sup>1,\*</sup> Pierre-Alexis Repecaud,<sup>2</sup> Yury Smirnov,<sup>2</sup> Lucas Atilla Bernardes Marçal,<sup>1</sup> Giovanni Fevola,<sup>3</sup> Dina Sheyfer,<sup>4</sup> Quentin Jeangros,<sup>5</sup> Wonsuk Cha,<sup>4</sup> Ross Harder,<sup>4</sup> Anders Mikkelsen,<sup>1</sup> Jesper Wallentin,<sup>1</sup> Monica Morales-Masis,<sup>2</sup> and Michael Elias Stuckelberger<sup>3</sup>

<sup>1</sup>*Division of Synchrotron Radiation Research and NanoLund,  
Department of Physics, Lund University,  
P.O. Box 118, SE-221 00 Lund, Sweden*

<sup>2</sup>MESA+ Institute for Nanotechnology,  
University of Twente, Enschede, 7500 AE, The Netherlands

<sup>3</sup>Centre for X-ray and Nano Science (CXNS),  
Deutsches Elektronen-Synchrotron DESY,  
Notkestraße 85, DE-22607 Hamburg, Germany

<sup>4</sup>APS, Argonne National Laboratory,

*9700 S Cass Ave, Lemont, IL 60439, United States*

<sup>5</sup>EPFL STI IMT PV-LAB, MC A2 238 (Bâtiment MC) Rue de la Maladière 71b,  
CP 526, CH-2002 Neuchâtel 2, Switzerland

(Dated: January 3, 2022)

## Abstract

Strain and interactions at grain boundaries during solid-phase crystallization are known to play a significant role in the functional properties of polycrystalline materials. However, elucidating three-dimensional nanoscale grain morphology, kinetics, and strain under realistic conditions is challenging. Here, we image a single-grain growth during the amorphous-to-polycrystalline transition in technologically relevant transparent conductive oxide (TCO) film of  $\text{In}_2\text{O}_3:\text{Zr}$  with *in-situ* Bragg coherent X-ray diffraction imaging and transmission electron microscopy. We find that the Johnson-Mehl-Avrami-Kolmogorov theory, which describes average kinetics of polycrystalline films growth, can be applied to the single grains as well. Quantitative analysis stems directly from imaging results. We elucidate the interface-controlled nature of the single-grain growth in thin films and reveal the surface strains which may be a driving force for anisotropic crystallization rates. Our results bring *in-situ* imaging with coherent X-rays towards understanding and controlling the crystallization processes of TCOs and other polycrystalline materials at nanoscale.

### **33 I. INTRODUCTION**

Polycrystalline materials are ubiquitous in materials science and engineering applications due to a wide variety of their functional properties. This includes metals, ceramics, oxides, and semiconductors. In polycrystalline bulk materials and thin films, grain structures and interfaces directly impact mechanical, optical, thermal, magnetic, electrical, and chemical properties due to the existence of local heterogeneity in structure, composition, chemistry, and electronic structure down to the atomic scale [1, 2]. These properties can be tuned by engineering the grain structures via mechanical, thermal, chemical, and other treatments. In this work, we consider an example of transparent conductive oxides (TCOs), widely accepted as transparent electrodes in a variety of high-performance devices, such as silicon heterojunction, copper indium gallium selenide, perovskite, and silicon-based tandem solar cells. In particular,  $\text{In}_2\text{O}_3$ -based TCOs doped with metals such as W, Ce, and Zr [3–6], have recently gained significant research attention due to their wide bandgap  $E_g$  and high electron mobilities  $\mu_e$ . It has been shown that these TCOs are mainly amorphous when deposited at room temperature and that their transport properties improve after solid-phase crystal-

---

\* [dmitry.dzhigaev@sljus.lu.se](mailto:dmitry.dzhigaev@sljus.lu.se)

lization by annealing at elevated temperatures [5, 7]. Studies of solid-phase crystallization phenomena in amorphous thin films are important for gaining new insights about the temporal structure-functionality relationship relevant to device optimization. Moreover, the strain fields developing both on the level of amorphous matrix and crystalline grains may drive the kinetics of crystallization. The general theory of the kinetics of phase change developed by Avrami [8] describes average characteristics of solid-phase crystallization. However, the details of growth and strain development on the scale of a single grains are lacking, limiting our understanding of the phenomenon. Three-dimensional (3D) nanoscale imaging of such processes *in situ* would improve our understanding of how grains grow, interact with each other and the substrates, and influence material properties.

The amorphous-to-polycrystalline transition in  $\text{In}_2\text{O}_3$ -based TCO films has been locally observed by top-view scanning electron microscopy with electron backscatter diffraction (EBSD) [3, 9], as well as by transmission electron microscopy (TEM) [7, 10]. These measurements were typically performed under *ex-situ* conditions without direct influence of reactive atmospheres and provide only 2D overview of the films, which may limit our understanding of the process. The crystallization dynamics of the whole thin film volume has been previously studied by *in-situ* X-ray diffraction (XRD) during the annealing experiments [3, 11, 12]. While electron microscopy provides close to atomic-scale resolution, the XRD technique allows following only the average crystal structure over large fields of view. Single-grain imaging with access to strain fields was realized by dark-field X-ray microscopy [13]. However, the spatial resolution has a lower limit of around 100 nm, the imaging setup requires high-quality lenses after the sample, and the strain sensitivity is limited.

Lensless Bragg coherent X-ray diffraction imaging (BCDI) addresses above-mentioned limitations by providing high-resolution 3D structure and strain in single nanoparticles under realistic conditions [14]. *In-situ* 3D imaging of annealing processes, defects formation, and phase transformations in grains and nanoparticles was demonstrated in a number of recent works [15–17]. The 3D diffraction patterns arising by coherent X-ray scattering from an isolated crystalline grain are highly sensitive to the shape and strain (down to  $10^{-4}$ ) [18, 19]. Therefore, BCDI is a highly suitable technique to study single-grain growth in polycrystalline materials.

Here, we apply *in-situ* 3D imaging of single grain growth during the Zr-doped  $\text{In}_2\text{O}_3$

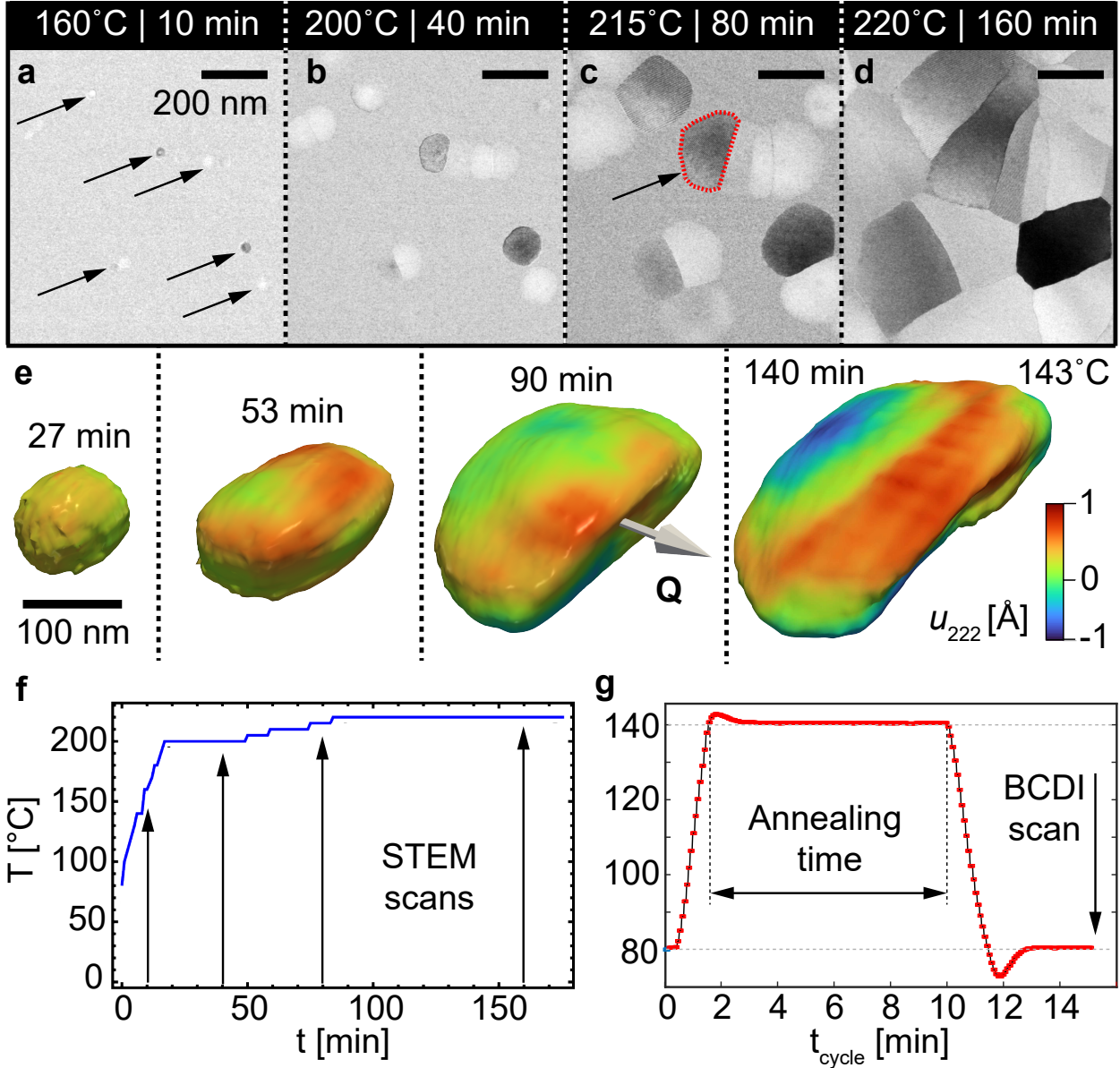


FIG. 1. (a-d) Scanning transmission electron microscopy (STEM) bright-field micrographs capturing the IZrO film crystallization process while heating in the microscope. Arrows in (a) indicate a selection of initial crystallites, while the grain highlighted by the red dashed contour in (c) exhibits a similar morphology to that analyzed by BCDI (see the full movie of the crystallization sequence in Supplementary Materials). (e) Three-dimensional BCDI reconstruction of a single grain growth during annealing of IZrO film. Color encodes displacement field  $\mathbf{u}_{222}(\mathbf{r})$ . The scattering vector  $\mathbf{Q}$ . Temperature profiles of the STEM measurement (f) and typical annealing cycle for the BCDI experiment (g).

80 (IZrO) film crystallization combined with *in-situ* TEM imaging [20] (see Figure 1a-e). We  
81 successfully performed 3D reconstructions of the single-grain morphology and strain evolu-  
82 tion starting from a sub-80 nm seed-particle up to its 400 nm fully crystallized state. We  
83 retrieved information about the initial stages of grain crystallization by direct analysis of  
84 the reciprocal space intensity distribution in the vicinity of the (222) Bragg reflection. 3D  
85 evolution of the grain shape and strain distribution was obtained by phase retrieval algo-  
86 rithms [21]. We applied high resolution TEM imaging to access a 2D overview of the same  
87 process in vacuum over many grains and obtained higher temporal and 2D spatial resolution.  
88 This correlative approach uniquely allows getting a more complete picture of the crystal-  
89 lization process. We evaluate the growth kinetics directly from imaging results employing  
90 the macroscopic Johnson-Mehl-Avrami-Kolmogorov (JMAK) theory on a single-grain level.  
91 This approach is a major step from the indirect analysis of XRD patterns reported previ-  
92 ously [10, 22]. Our quantitative analysis of the morphology kinetics and strain development  
93 lays the experimental foundation for more detailed theories of solid-phase crystallization  
94 phenomena.

## 95 II. RESULTS

### 96 A. Sample

97 Amorphous IZrO films were prepared by Pulsed Laser Deposition (PLD) at room temper-  
98 ature (see Methods for details). The films are 100 nm thick and present good optoelectronic  
99 properties (bandgap:  $E_g > 3.5$  eV; electron mobility  $> 20 \text{ cm}^2/\text{Vs}$  and free carrier density  
100 of  $4^{20} \text{ cm}^{-3}$ ). Annealing at temperatures above 150 °C in air results in solid-phase crys-  
101 tallization of the films, leading to polycrystalline films with large grains, further improving  
102 the optoelectronic properties of the films: widening of the bandgap ( $E_g > 3.7$  eV) and the  
103 increase of electron mobility ( $\mu_e > 70 \text{ cm}^2/\text{Vs}$ ) [5, 7, 9].

### 104 B. *In-situ* 2D imaging of IZrO solid-phase crystallization via TEM

105 We first investigated the microstructure and crystallization kinetics of IZrO thin films by  
106 scanning TEM (see Methods for details). The as-deposited IZrO films feature small crys-  
107 tallites dispersed in an amorphous matrix (see arrows in Figure 1a). The crystallites then

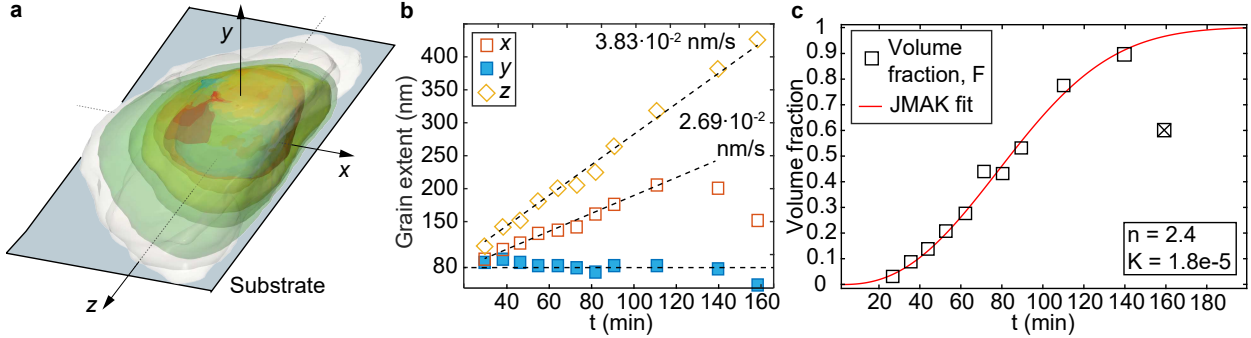


FIG. 2. Morphology and growth kinetics of a single IZrO grain. (a) Isosurfaces of amplitude  $\rho(\mathbf{r})$  represent the time steps and corresponding BCDI reconstruction. All reconstructions are aligned with respect to their center of masses. The sample reference frame ( $x, y, z$ ) is aligned with substrate and principal growth directions of the grain. (b) Time dependence of the grain dimensions in the sample reference frame. Rates correspond to linear fits shown by dashed lines. (c) The volume fraction  $F$  of the IZrO grain as a function of annealing time obtained from BCDI reconstructions (black squares). The solid red line is the nonlinear fitting curve to the JMAK equation obtained by the trust-region algorithm (R-square: 0.9884).

108 grow upon annealing inside the microscope (see Figure 1b, c) according to the temperature  
 109 profile shown in Figure 1f. The TEM micrographs demonstrate a complicated picture of the  
 110 single grain interaction with neighbors during growth. The final image shows a dense state  
 111 of the resulting polycrystalline IZrO film (see Figure 1d). The film crystallizes according  
 112 to the bixbyite  $\text{In}_2\text{O}_3$  crystal structure, as highlighted by the atomic resolution image and  
 113 the corresponding fast Fourier transform (see Figure S2 in Supplementary Information).  
 114 Extending this first steady-state microstructural picture, we utilized *in-situ* BCDI to investi-  
 115 giate the crystallization process in 3D and assess strain fields. Note that the *in-situ* TEM  
 116 experiment was performed in a high vacuum ( $10^{-7}$  mbar), which may lead to differences in  
 117 the crystallization kinetics compared to the air-annealed BCDI experiment shown below [7].

### 118 C. *In-situ* 3D imaging of IZrO solid-phase crystallization via BCDI

119 We applied the BCDI technique to image the evolution of a single grain during the crys-  
 120 tallization process. This yields the 3D structure and strain fields, complementary to electron  
 121 microscopy that provides high spatial resolution in 2D. Our experiment was conducted un-

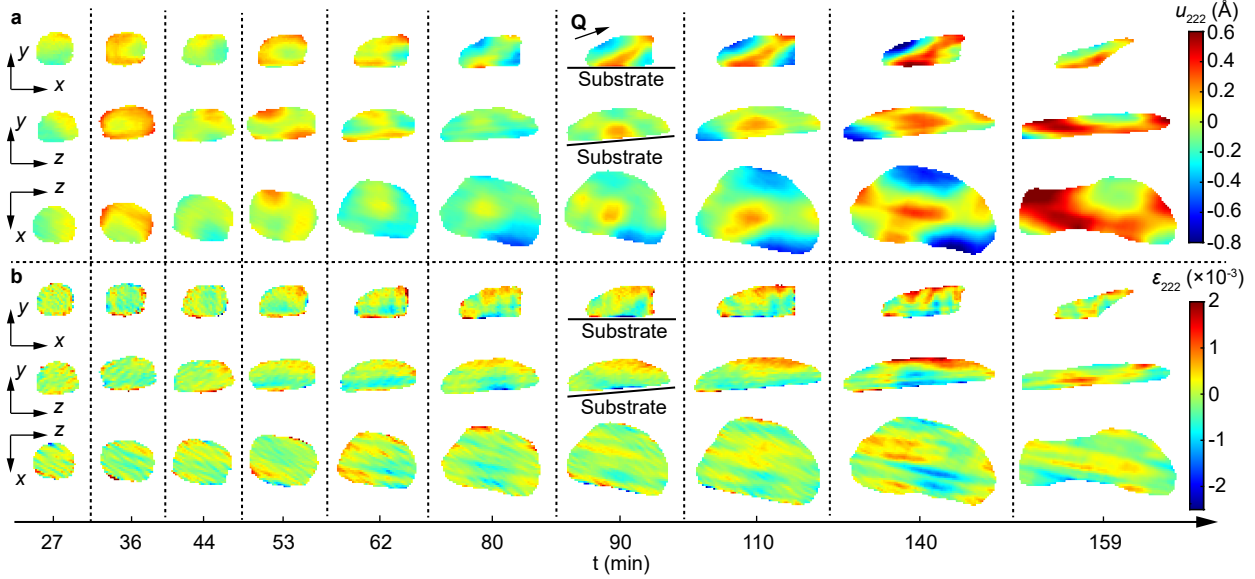


FIG. 3. Orthogonal cuts through the 3D displacement (a) and strain fields (b) obtained with BCDI reconstruction of the IZrO grain as a function of annealing time. The scattering vector  $\mathbf{Q}$  is shown in the panel (a) at 90 min. The lengths of coordinate axes correspond to 100 nm scale.

122 der isothermal annealing conditions (see Methods for details). First, the film was heated up  
 123 to 81 °C from room temperature. The annealing cycle consisted of (1) a temperature ramp  
 124 from 81 °C to 143 °C at 50 °C/min rate, (2) the actual annealing step at 143 °C, (3) the  
 125 cooling down to 81 °C, initiated 10 min after starting the cycle, and (4) keeping the sample  
 126 at 81 °C for the BCDI measurement. An example of the temperature profile is shown in  
 127 Figure 1g. A moderate annealing temperature of 143 °C was chosen to provide precise con-  
 128 trol over the rate of crystallization. The number of BCDI measurements was only limited  
 129 by the available beamtime. The total annealing time was about 160 min, which corresponds  
 130 to 80-90 % of crystallization at 143 °C [10]. After each annealing sequence, we recorded 3  
 131 consecutive BCDI scans at 81 °C by performing slight sample tilts in the vicinity of (222)  
 132 Bragg condition and recording far-field diffraction patterns on the 2D detector.

134 In total, 13 BCDI datasets were measured for the case of time-dependent annealing of a  
 135 single IZrO grain. The first two datasets contain no coherent fringes due to a small grain  
 136 size at the initial steps of crystallization. In these cases the upper limit on the grain size  
 137 was estimated by employing the Scherrer equation [23] (see Supplementary Information for  
 138 details). The seed particle size is estimated to be 55×75 nm (x,y) after 8 min of annealing.  
 139 The second dimension matches well with the thickness of the deposited film. The growth of

<sup>140</sup> the grain continued further in the  $xz$ -plane and is analyzed in the following section starting  
<sup>141</sup> from 26 min of annealing.

<sup>142</sup> The 3D complex-valued density of the grain  $\rho(\mathbf{r})$  was reconstructed in direct space by  
<sup>143</sup> inverting 3D diffraction data using iterative phase retrieval algorithms [19, 21], as in the  
<sup>144</sup> selected reconstructions shown in Figure 1e. The modulus of this function defines the shape  
<sup>145</sup> of the grain and is proportional to the electron density of selected crystal planes. The phase  
<sup>146</sup> of  $\rho(\mathbf{r})$  is linearly proportional to the displacement field  $u(\mathbf{r})$  of atoms from their equilibrium  
<sup>147</sup> positions as  $\varphi(\mathbf{r}) = -\mathbf{Q} \cdot \mathbf{u}(\mathbf{r})$ , where  $\mathbf{Q}$  is the scattering vector [24].

<sup>148</sup> The isosurfaces of reconstruction at 25 % of the maximum amplitude value allow for  
<sup>149</sup> surface morphology evaluation (see Figure 2a). We observe that every reconstruction  $\rho_i$   
<sup>150</sup> is well contained by the next one in time  $\rho_{i+1}$ . We were able to track the growth of a  
<sup>151</sup> single particle thanks to the unique ability of BCDI to keep track of a particular grain in  
<sup>152</sup> a polycrystalline material. A clear vertical facet perpendicular to the substrate plane was  
<sup>153</sup> observed in the reconstructed crystal. We attribute this feature to a grain boundary, similar  
<sup>154</sup> to those revealed by TEM measurements in Figure 1a. The  $\mathbf{Q}$ -vector is oriented at  $19^\circ$  with  
<sup>155</sup> respect to the normal of the facet, suggesting that the boundary is (211)-oriented.

<sup>156</sup> The growth rates along the facets of the grain were evaluated by extracting corresponding  
<sup>157</sup> profiles of the amplitudes  $|\rho_i|$  and calculating the width at 25 % threshold (see Figure 2b).  
<sup>158</sup> The thickness of the grain reaches the average value of  $80.7 \pm 5$  nm along the  $y$ -axis, which  
<sup>159</sup> is well within the experimental error of the thickness measurement that yielded 78 nm for  
<sup>160</sup> the as-deposited amorphous film. No additional growth was observed along  $y$  after 27 min.  
<sup>161</sup> Crystallization rates along orthogonal  $x$  and  $z$  directions are linear and have corresponding  
<sup>162</sup> values of  $2.69 \cdot 10^{-2}$  nm/s and  $3.83 \cdot 10^{-2}$  nm/s. The last 2 points in the case of  $x$ -direction  
<sup>163</sup> deviate from linear dependence due to the interaction with adjacent grains.

<sup>164</sup> The volume  $V$  of the particle was evaluated by calculating the number of voxels fitting  
<sup>165</sup> into a 3D hull at 25 % of the amplitude. The corresponding normalized volume change  
<sup>166</sup>  $F = V/\max(V)$  with time is shown in Figure 2c. The grain volume increases almost linearly  
<sup>167</sup> with time, except for the last point where a part of the crystal was damaged/tilted and did  
<sup>168</sup> not contribute to the Bragg peak intensity anymore.

169     D. Kinetics of grain growth

170     In the case of bcc  $\text{In}_2\text{O}_3$  free micro-particles, the growth directions are determined by  
171     energies of the low index facets  $\gamma_{111} < \gamma_{001} < \gamma_{110}$  [25]. However, this relation is violated in  
172     the complex interplay between the substrate, neighboring grains, and amorphous matrix.

173     Under isothermal conditions, the thermodynamics determining the nucleation and growth  
174     is expected to be constant, and the fractional amount of crystallization as a function of time  
175      $F(t)$  can be described by the Avrami (JMAK) equation [8],

$$F(t) = 1 - \exp(-Kt^n), \quad (1)$$

176     where  $K$  is a temperature-dependent constant related to the nucleation and growth rates  
177     of the crystalline phase. The second constant,  $n$ , is the kinetic or Avrami exponent, which  
178     indicates the mechanisms of the amorphous-to-crystalline transition, its dimensionality, and  
179     typically has values between 1 and 4 [26]. We stress that this model describes an averaged  
180     behavior of polycrystalline materials and has not been tested on a single grain level. Impor-  
181     tantly, in the case of BCDI reconstructions we have direct access to the crystalline volume  
182     of the crystal-amorphous system confined by the interaction volume between the sample  
183     and the X-ray beam. Therefore, the fraction can be obtained as a normalized volume of  
184     the grain  $F$ . The JMAK curve was fitted to our experimental data with the maximum  $F$   
185     value reaching 90 % of crystallization (see Figure 2c). This assumption is supported by the  
186     fact that the last data point was measured when the grain impinged adjacent crystallites  
187     and consequently deformed. The resulting fitting parameter values are  $K = 1.6 \cdot 10^{-5}$  and  
188      $n = 2.4$  (see Methods for details). These values are in good agreement with the reports for  
189     indium oxide films studied by XRD and accessing averaged structure and dynamics [9, 10].  
190     With this quantitative analysis we can conclude that a single-grain growth as measured  
191     by BCDI follows the growth kinetics which can be described by JMAK theory applied di-  
192     rectly to imaging results. Moreover, *in-situ* BCDI directly accesses strain fields and grain  
193     deformation as a function of annealing time, which becomes more important in the light  
194     of TCO thickness reduction in solar cells or ever-shrinking scales of nanodevices employing  
195     TCOs [27, 28].

196     Further, we analyzed the spatial distribution of local crystal deformation that may affect  
197     the growth of a single grain. The 3D displacement field was extracted from the phase of the

198 object as  $u_{222}(\mathbf{r}) = -\varphi(\mathbf{r})/|\mathbf{Q}|$ . The corresponding strain fields were calculated as

$$\varepsilon_{222}(\mathbf{r}) = \nabla \mathbf{u}(\mathbf{r}) \cdot \hat{\mathbf{n}}_Q, \quad (2)$$

199 where  $\hat{\mathbf{n}}_Q = \mathbf{Q}/|\mathbf{Q}|$  is a unit vector. The orthogonal cuts through the displacement and  
200 strain fields are shown in Figure 3. The displacement field maps demonstrate local variation  
201 patterns that are traceable throughout the crystallization snapshots. As the annealing pro-  
202 ceeded, the absolute values of  $u_{222}$  increased and lead to plastic deformation of the grain at  
203 the last step. The orthogonal cuts through 3D strain distributions reveal compressive strain  
204 at the substrate-grain boundary. Most of the outer surface of the grain shows tensile strain,  
205 especially over the second half of the annealing process. A more detailed picture of the  
206 strain evolution was extracted in line profiles along sample axes  $x, y, z$  shown in Figure 4.  
207 The edge enhancement of absolute strain values is visible in each set of profiles. In the case  
208 of out-of-plane direction, Figure 4a, we observed the change of the strain from tensile to  
209 compressive at the crystallite/substrate interface (shown by arrows), revealing a complex  
210 interplay between grain surface energy and interaction with neighboring particles and the  
211 amorphous matrix. Correspondingly, the interface-controlled growth may be affected by the  
212 strain building up at the boundaries.

213 The accuracy of the BCDI reconstructions is limited by spatial resolution and time sam-  
214 pling. Moreover, the spatial resolution is not a constant value throughout the measurement  
215 of the particle with increasing volume and highly anisotropic due to the asymmetric shape  
216 of the grain. The spatial resolution of the reconstruction varies from 50 nm to below 20 nm,  
217 as it was estimated by evaluating line spread functions at the known edges of the particle  
218 (see Supplementary Information for details).

220 With the demonstrated approach, we foresee statistically more significant measurements  
221 will be possible at 4<sup>th</sup> generation synchrotron sources including Advanced Photon Source  
222 Upgrade Project [29], PETRA IV [30], ESRF-EBS [31], MAX IV [32]. With increased  
223 coherent photon flux, faster scans will become possible with improved spatial and temporal  
224 resolution. Specifically, one could access the initial stages of crystallites nucleation, when  
225 the sizes of the particles are below 50 nm. The method of *in-situ* BCDI is relevant to other  
226 grain-growth phenomena, such as, for example, Ostwald ripening [33].

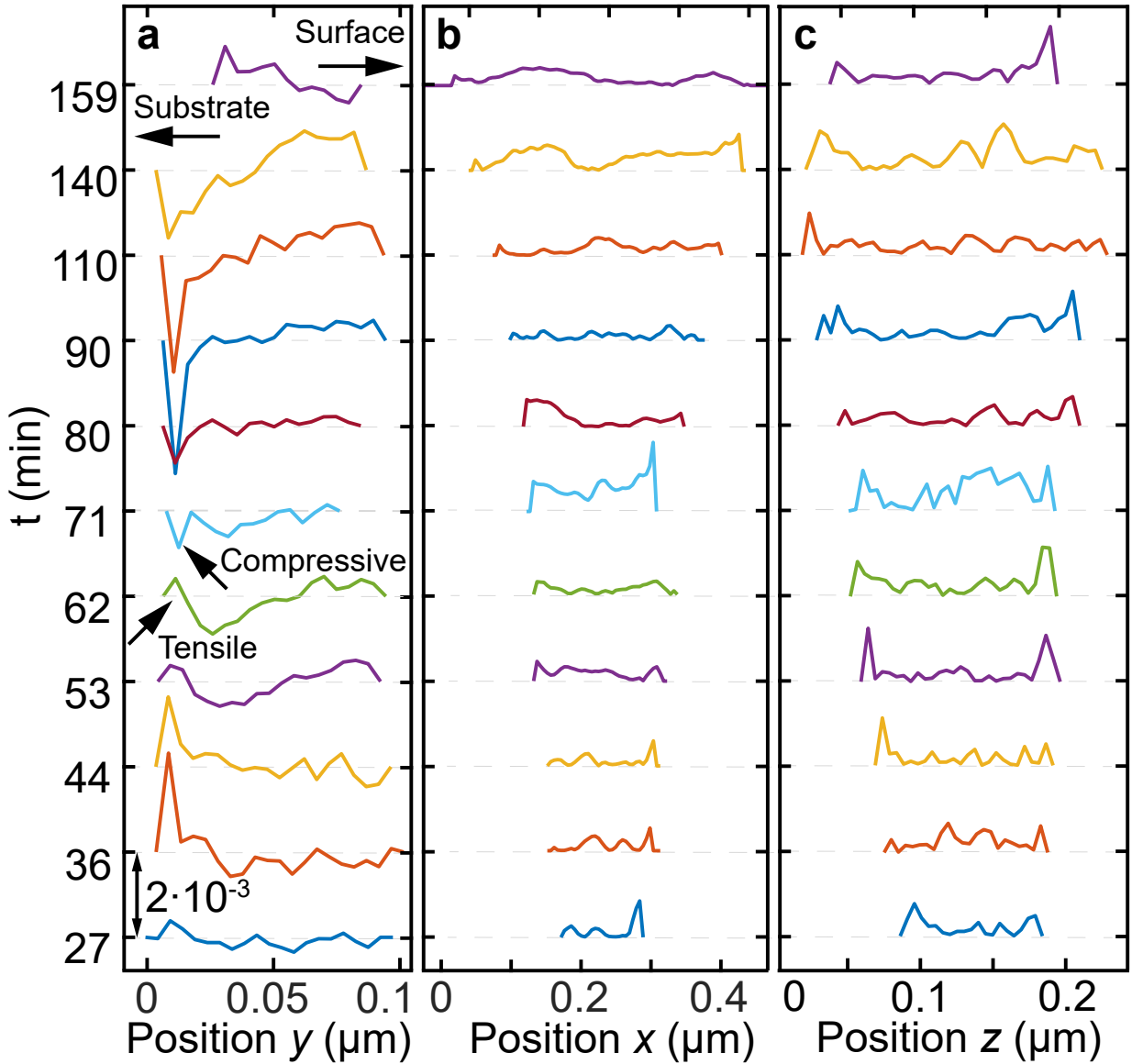


FIG. 4. Line profiles of the strain extracted from BCDI reconstructions at each time step in the annealing process. The directions correspond to those in Figure 2a. All the graphs are on the same scale with a constant shift of  $2 \cdot 10^{-3}$  for clarity.

<sup>227</sup> **III. CONCLUSION**

<sup>228</sup> In conclusion, we performed 3D *in-situ* imaging of single-grain growth in a functional  
<sup>229</sup> polycrystalline TCO film. We devised an approach for analysis of kinetics of a single-grain  
<sup>230</sup> growth directly from 3D BCDI results, extending the applicability of JMAK theory of solid-  
<sup>231</sup> phase crystallization. With the advance of 4<sup>th</sup> generation synchrotron sources and X-ray

232 free-electron lasers, the earlier stages of crystallization will be accessible and spatiotemporal  
233 resolution significantly improved. Combined with advanced phasing algorithms and machine  
234 learning approaches for rapid data analysis, *in-situ* BCDI is a powerful tool for nanoscale  
235 characterization of dynamics in polycrystalline materials.

236 **METHODS**

237 **A. Preparation of IZrO thin films**

238 IZrO thin films were fabricated by wafer-based PLD at room temperature onto monocrys-  
239 talline Si substrates in planar configuration coated with hydrogenated amorphous Silicon  
240 (a-Si:H) layers deposited via plasma-enhanced chemical vapor deposition (similar substrates  
241 are used for SHJ solar cell fabrication[34]). The IZrO target (98/2 wt%  $\text{In}_2\text{O}_3/\text{ZrO}_2$ ) was  
242 ablated with KrF excimer laser ( $\lambda=248$  nm) with the repetition rate of 20 Hz and the fluence  
243 of  $1.9 \text{ J/cm}^2$ . The total working pressure was 0.02 mbar with an oxygen total flow ratio  
244  $r(\text{O}_2) = Q(\text{O}_2)/(Q(\text{Ar} + \text{O}_2)$  of 20 % as demonstrated previously [9]. The thickness of the  
245 IZrO layer was 78 nm as derived from the surface step height obtained by stylus profilometry  
246 measurements.

247 **B. Scanning transmission electron microscopy**

248 The sample dedicated for TEM analysis was deposited by PLD directly on a microelec-  
249 tromechanical systems (MEMS) chip with heating capabilities (from DENSSolutions [35]).  
250 The IZrO-coated MEMS chip was mounted on a double-tilt holder and introduced in an  
251 image- and probe-corrected Thermo Fisher Scientific Titan Themis electron microscope.  
252 Experiments were performed in STEM mode at 200 kV with a probe current of 400 pA.

253 **C. Synchrotron experiment**

254 The BCDI measurements were performed remotely with minimal intervention from the  
255 beamline staff at the 34-ID-C beamline at the Advanced Photon Source (Argonne National  
256 Laboratory, USA). The amorphous IZrO film was mounted on a heater cell available at the  
257 beamline. The temperature values presented in this work were calibrated before the BCDI

258 experiment (see Table S1 in Supplementary Information). An X-ray beam with a photon  
259 energy of 9 keV ( $\lambda = 1.38 \text{ \AA}$ ) was focused down to  $800 \text{ nm} \times 600 \text{ nm}$  ( $h \times v$ ) at full width at  
260 half maximum using Kirkpatrick–Baez mirrors [36]. The Timepix 2D detector (Amsterdam  
261 Scientific Instruments) with a GaAs sensor and pixel size of  $55 \mu\text{m} \times 55 \mu\text{m}$  was positioned  
262 at the double Bragg angle  $2\theta_B \approx 27^\circ$  of the (222) reflection of IZrO. The distance from the  
263 sample to the detector was adjusted during the measurements to ensure that the diffraction  
264 patterns were oversampled [37]. The incoming X-ray beam had a fixed low incidence angle of  
265  $5^\circ$  to maximize the footprint on the sample. The focal spot size of the X-ray beam was large  
266 enough to fully illuminate grains up to 500 nm in scale (see Methods for further details).  
267 This geometry allowed for fast scanning of films at fixed detector position and increased  
268 the probability of finding (222)-oriented seed particles. The signal from seed particles was  
269 recognized by faint Bragg peaks appearing on the 2D detector during the scan. The BCDI  
270 scans were generally performed in the angular range of  $0.6^\circ$  with a step size of  $0.006^\circ$ . At each  
271 annealing step, at least 3 rocking curves were recorded with realignment scans in-between.  
272 Thermal expansion of the sample stage and IZrO crystal was compensated by realignment  
273 of scanning and rocking curve motors at each step of temperature change. The Bragg peak  
274 was always positioned close to the center of detector module to avoid gaps in the recorded  
275 data. The resulting datasets were aligned in 3D with sub-pixel accuracy[38] based on the  
276 maximum cross-correlation coefficient and summed up later to improve the signal-to-noise  
277 ratio in the data.

278     **D. Sample post-characterization**

279     We performed additional electron back-scattering (EBSD) measurement after the beam-  
280 time at DESY Nanolab [39]. It proved the polycrystalline nature of the IZrO film (see  
281 Supplementary Information for details). XRD was performed on the same sample at the  
282 laboratory source at Lund University and revealed bixbyite  $\text{In}_2\text{O}_3$  crystal structure (see  
283 Supplementary Information for details).

284      **E. Phase retrieval**

285      The iterative phase retrieval was performed by employing the combination of Error-  
286      Reduction (ER), Hybrid Input-Output (HIO) algorithms, and guided approach for 5 gen-  
287      erations, with a population of 10 per generation [21, 40]. The selection rule for the best  
288      candidate of the complex-valued object  $\rho_i(\mathbf{r})$  in each generation was based on the high-  
289      est value of sharpness metric  $S = \sum |\rho(\mathbf{r})|^4$  and breeding of new estimates of the object  
290      for the new generation is calculated as  $\rho_i^*(\mathbf{r}) = \sqrt{\rho_i(\mathbf{r})\rho_{best}(\mathbf{r})}$ . The final error-metric  
291       $E = \sum_Q |||\mathcal{F}(\rho(\mathbf{Q}))|^2 - I(\mathbf{Q})||$  reached the lowest value of about 2 % in the case of both  
292      domains. The complex-conjugate solutions to the phase retrieval problem were filtered in  
293      the direct space by the orientation of flat facet of the grain since it is expected to be fac-  
294      ing Si substrate. The phase ramps were removed from the reconstructed objects before  
295      quantitative analysis.

296      **F. Kinetics of grain growth**

297      In general, the Avrami exponent  $n = 2.4$  is not constant during the crystallization and can  
298      be expanded in the following form [41]  $n = b + pm$ , where  $b$  is the nucleation index,  $p$  is the  
299      growth index between 0.5 and 1, and  $m$  denotes the  $d$ -dimensional grain growth. In our case,  
300       $b = 0$  since there is only a single nucleation event,  $m \approx 2$  since the 3D growth is limited  
301      by the thickness of the amorphous film, and  $p = 1$  since the growth is mainly interface-  
302      controlled [10]. In polycrystalline thin films, the grain growth does not strictly follow classical  
303      JMAK theory, therefore the local values of the Avrami exponent as a function of crystalline  
304      fraction  $n(F)$  were evaluated following Ref. [42] (see Supplementary Information for details).  
305      The mean value of  $\langle n(F) \rangle = 2.5$  is remarkably close to the one obtained by JMAK fit of  
306      crystalline fraction, while providing values of around 4 at the beginning of the process. It  
307      is important to note that the exact values of the extracted parameters may differ due to  
308      additional crystallization happening during temperature ramp-up/-down (see Figure 1g).  
309      The crystallization rates are expected to be much lower in these regions and annealing time

<sup>310</sup> may be increased by 1-2 min.

---

- <sup>311</sup> [1] Michael F Ashby, Hugh Shercliff, and David Cebon. *Materials: engineering, process-*  
<sup>312</sup> *ing and design*. Butterworth-Heinemann, 2018.
- <sup>313</sup> [2] A. Ulvestad, S. O. Hruszkewycz, M. V. Holt, M. O. Hill, I. Calvo-Almazán, S. Maddali,  
<sup>314</sup> X. Huang, H. Yan, E. Nazaretski, Y. S. Chu, L. J. Lauhon, N. Rodkey, M. I. Bertoni, and  
<sup>315</sup> M. E. Stuckelberger. Multimodal X-ray imaging of grain-level properties and performance in  
<sup>316</sup> a polycrystalline solar cell. *Journal of Synchrotron Radiation*, 26(4):1316–1321, Jul 2019.
- <sup>317</sup> [3] Takashi Koida, Yuko Ueno, and Hajime Shibata. In<sub>2</sub>O<sub>3</sub>-based transparent conducting oxide  
<sup>318</sup> films with high electron mobility fabricated at low process temperatures. *Physica Status Solidi*  
<sup>319</sup> (a), 215(7):1700506, 2018.
- <sup>320</sup> [4] Monica Morales-Masis, Esteban Rucavado, Raphaël Monnard, Loris Barraud, Jakub Holovsky,  
<sup>321</sup> Matthieu Despeisse, Mathieu Boccard, and Christophe Ballif. Highly conductive and broad-  
<sup>322</sup> band transparent zr-doped In<sub>2</sub>O<sub>3</sub> as front electrode for solar cells. *IEEE Journal of Photo-*  
<sup>323</sup> *voltaics*, 8(5):1202–1207, 2018.
- <sup>324</sup> [5] Erkan Aydin, Michele De Bastiani, Xinbo Yang, Muhammad Sajjad, Faisal Aljamaan, Yury  
<sup>325</sup> Smirnov, Mohamed Nejib Hedhili, Wenzhu Liu, Thomas G Allen, Lujia Xu, et al. Zr-doped  
<sup>326</sup> indium oxide (IZRO) transparent electrodes for perovskite-based tandem solar cells. *Advanced*  
<sup>327</sup> *functional materials*, 29(25):1901741, 2019.
- <sup>328</sup> [6] Leonard Tutsch, Hitoshi Sai, Takuya Matsui, Martin Bivour, Martin Hermle, and Takashi  
<sup>329</sup> Koida. The sputter deposition of broadband transparent and highly conductive cerium and  
<sup>330</sup> hydrogen co-doped indium oxide and its transfer to silicon heterojunction solar cells. *Progress*  
<sup>331</sup> *in Photovoltaics: Research and Applications*, 2021.
- <sup>332</sup> [7] Esteban Rucavado, Federica Landucci, Max Döbeli, Quentin Jeangros, Mathieu Boccard,  
<sup>333</sup> Aïcha Hessler-Wyser, Christophe Ballif, and Monica Morales-Masis. Zr-doped indium oxide  
<sup>334</sup> electrodes: Annealing and thickness effects on microstructure and carrier transport. *Physical*  
<sup>335</sup> *Review Materials*, 3(8):084608, 2019.
- <sup>336</sup> [8] M Avrami. General theory. *J. Chem. Phy.*, 7:103–112, 1939.
- <sup>337</sup> [9] Yury Smirnov, Laura Schmengler, Riemer Kuik, Pierre-Alexis Repecaud, Mehrdad Najafi,  
<sup>338</sup> Dong Zhang, Mirjam Theelen, Erkan Aydin, Sjoerd Veenstra, Stefaan De Wolf, et al. Scal-

- 339 able pulsed laser deposition of transparent rear electrode for perovskite solar cells. *Advanced*  
340 *Materials Technologies*, 6(2):2000856, 2021.
- 341 [10] Junjun Jia, Shimpei Iwasaki, Shingo Yamamoto, Shin-ichi Nakamura, Eisuke Magome, Toshi-  
342 hiro Okajima, and Yuzo Shigesato. Temporal evolution of microscopic structure and function-  
343 ality during crystallization of amorphous indium-based oxide films. *ACS Applied Materials &*  
344 *Interfaces*, 13(27):31825–31834, 2021.
- 345 [11] Hans F Wardenga, Mareike V Frischbier, Monica Morales-Masis, and Andreas Klein. In situ  
346 hall effect monitoring of vacuum annealing of  $\text{In}_2\text{O}_3$ : H thin films. *Materials*, 8(2):561–574,  
347 2015.
- 348 [12] Meihan Wang, Yutaka Sawada, Hao Lei, Yoshiyuki Seki, Yoichi Hoshi, Takayuki Uchida,  
349 Takayuki Konya, and Akira Kishi. Thermal crystallization kinetics and crystallite size dis-  
350 tribution of amorphous ITO film deposited in the presence or absence of water vapor. *Thin*  
351 *Solid Films*, 518(11):2992–2995, 2010.
- 352 [13] Hugh Simons, A King, Wolfgang Ludwig, C Detlefs, Wolfgang Pantleon, Søren Schmidt,  
353 F Stöhr, I Snigireva, A Snigirev, and Henning Friis Poulsen. Dark-field x-ray microscopy for  
354 multiscale structural characterization. *Nature communications*, 6(1):1–6, 2015.
- 355 [14] Mark A Pfeifer, Garth J Williams, Ivan A Vartanyants, Ross Harder, and Ian K Robinson.  
356 Three-dimensional mapping of a deformation field inside a nanocrystal. *Nature*, 442(7098):63–  
357 66, 2006.
- 358 [15] Andrew Ulvestad, Andrej Singer, JN Clark, HM Cho, Jong Woo Kim, Ross Harder, Jorg  
359 Maser, YS Meng, and OG Shpyrko. Topological defect dynamics in operando battery nanopar-  
360 ticles. *Science*, 348(6241):1344–1347, 2015.
- 361 [16] Allison Yau, Wonsuk Cha, Matthew W Kanan, G Brian Stephenson, and Andrew Ulvestad.  
362 Bragg coherent diffractive imaging of single-grain defect dynamics in polycrystalline films.  
363 *Science*, 356(6339):739–742, 2017.
- 364 [17] David Yang, Nicholas W Phillips, Kay Song, Ross J Harder, Wonsuk Cha, and Felix Hofmann.  
365 Annealing of focused ion beam damage in gold microcrystals: an in situ bragg coherent x-ray  
366 diffraction imaging study. *Journal of Synchrotron Radiation*, 28(2), 2021.
- 367 [18] Ian Robinson and Ross Harder. Coherent x-ray diffraction imaging of strain at the nanoscale.  
368 *Nature materials*, 8(4):291–298, 2009.

- [369] [19] Jesse N Clark, Johannes Ihli, Anna S Schenk, Yi-Yeoun Kim, Alexander N Kulak, James M  
[370] Campbell, Gareth Nisbet, Fiona C Meldrum, and Ian K Robinson. Three-dimensional imaging  
[371] of dislocation propagation during crystal growth and dissolution. *Nature Materials*, 14(8):780–  
[372] 784, 2015.
- [373] [20] Mahyar M Moghadam, Ran Li, D Bruce Buchholz, Qianqian Li, Peter W Voorhees, and  
[374] Vinayak P Dravid. In situ crystallization and morphological evolution in multicomponent  
[375] indium oxide thin films. *Crystal Growth & Design*, 17(3):1396–1403, 2017.
- [376] [21] James R Fienup. Phase retrieval algorithms: a personal tour. *Applied optics*, 52(1):45–56,  
[377] 2013.
- [378] [22] Bart Macco, Marcel A Verheijen, Lachlan E Black, Beatriz Barcones, J Melskens, and Wil-  
[379] helmus MM Kessels. On the solid phase crystallization of  $\text{In}_2\text{O}_3$ : H transparent conductive  
[380] oxide films prepared by atomic layer deposition. *Journal of Applied Physics*, 120(8):085314,  
[381] 2016.
- [382] [23] AL Patterson. The scherrer formula for x-ray particle size determination. *Physical review*,  
[383] 56(10):978, 1939.
- [384] [24] D Dzhigaev, A Shabalin, T Stankevič, U Lorenz, RP Kurta, F Seiboth, J Wallentin, A Singer,  
[385] S Lazarev, OM Yefanov, et al. Bragg coherent x-ray diffractive imaging of a single indium  
[386] phosphide nanowire. *Journal of Optics*, 18(6):064007, 2016.
- [387] [25] Ming Meng, Xinglong Wu, Xiaobin Zhu, Lun Yang, Zhixing Gan, Xiaoshu Zhu, Lizhe Liu, and  
[388] Paul K Chu. Cubic  $\text{In}_2\text{O}_3$  microparticles for efficient photoelectrochemical oxygen evolution.  
[389] *The journal of physical chemistry letters*, 5(24):4298–4304, 2014.
- [390] [26] Weixue Li and Tzuchiang Wang. Ab initio investigation of the elasticity and stability of  
[391] aluminium. *Journal of Physics: Condensed Matter*, 10(43):9889, 1998.
- [392] [27] Jesper Wallentin, Nicklas Anttu, Damir Asoli, Maria Huffman, Ingvar Åberg, Martin H Mag-  
[393] nusson, Gerald Siefer, Peter Fuss-Kailuweit, Frank Dimroth, Bernd Witzigmann, et al. InP  
[394] nanowire array solar cells achieving 13.8% efficiency by exceeding the ray optics limit. *Science*,  
[395] 339(6123):1057–1060, 2013.
- [396] [28] Gaute Otnes, Enrique Barrigón, Christian Sundvall, K Erik Svensson, Magnus Heurlin, Ger-  
[397] ald Siefer, Lars Samuelson, Ingvar Åberg, and Magnus T Borgström. Understanding InP  
[398] nanowire array solar cell performance by nanoprobe-enabled single nanowire measurements.  
[399] *Nano letters*, 18(5):3038–3046, 2018.

- 400 [29] Thomas E Fornek. Advanced photon source upgrade project final design report. Technical  
401 report, Argonne National Lab.(ANL), Argonne, IL (United States), 2019.
- 402 [30] Christian G Schroer, Ilya Agapov, Werner Brefeld, Reinhard Brinkmann, Y-C Chae, H-C  
403 Chao, Mikael Eriksson, Joachim Keil, Xavier Nuel Gavaldà, Ralf Röhlsberger, et al. PE-  
404 TRA IV: the ultralow-emittance source project at DESY. *Journal of synchrotron radiation*,  
405 25(5):1277–1290, 2018.
- 406 [31] Pantaleo Raimondi. ESRF-EBS: The extremely brilliant source project. *Synchrotron Radia-*  
407 *tion News*, 29(6):8–15, 2016.
- 408 [32] Pedro F Tavares, Eshraq Al-Dmour, Åke Andersson, Francis Cullinan, Brian N Jensen, David  
409 Olsson, David K Olsson, Magnus Sjöström, Hamed Tarawneh, Sara Thorin, et al. Commis-  
410 sioning and first-year operational results of the MAX IV 3 GeV ring. *Journal of synchrotron*  
411 *radiation*, 25(5):1291–1316, 2018.
- 412 [33] Wilhelm Ostwald. Studien über die bildung und umwandlung fester körper. *Zeitschrift für*  
413 *physikalische Chemie*, 22(1):289–330, 1897.
- 414 [34] Martin Bivour, Sebastian Schröer, Martin Hermle, and Stefan W Glunz. Silicon heterojunction  
415 rear emitter solar cells: Less restrictions on the optoelectrical properties of front side tcos.  
416 *Solar energy materials and solar cells*, 122:120–129, 2014.
- 417 [35] DENSSolutions. <https://denssolutions.com/>.
- 418 [36] Paul Kirkpatrick and Albert Vincio Baez. Formation of optical images by x-rays. *JOSA*,  
419 38(9):766–774, 1948.
- 420 [37] David Sayre. Some implications of a theorem due to shannon. *Acta Crystallographica*,  
421 5(6):843–843, 1952.
- 422 [38] Manuel Guizar-Sicairos, Samuel T Thurman, and James R Fienup. Efficient subpixel image  
423 registration algorithms. *Optics letters*, 33(2):156–158, 2008.
- 424 [39] Andreas Stierle, Thomas F Keller, Heshmat Noei, Vedran Vonk, and Ralf Roehlsberger. DESY  
425 nanolab. *Journal of large-scale research facilities JLSRF*, 2:76, 2016.
- 426 [40] A Ulvestad, Y Nashed, Guillaume Beutier, M Verdier, SO Hruszkewycz, and M Dupraz.  
427 Identifying defects with guided algorithms in bragg coherent diffractive imaging. *Scientific*  
428 *reports*, 7(1):1–9, 2017.
- 429 [41] Qian Gao, Zengyun Jian, Junfeng Xu, Man Zhu, Fange Chang, and Amin Han. Crystallization  
430 kinetics of the Cu<sub>50</sub>Zr<sub>50</sub> metallic glass under isothermal conditions. *Journal of Solid State*

- 431        *Chemistry*, 244:116–119, 2016.
- 432        [42] A Calka and AP Radlinski. The local value of the Avrami exponent: a new approach to  
433        devitrification of glassy metallic ribbons. *Materials Science and Engineering*, 97:241–246,  
434        1988.

435        **ACKNOWLEDGMENTS**

436        This work was performed with help from the NanoLund Centre for Nanoscience at Lund  
437        University, and was supported by the Swedish Research Council (VR), and the Swedish  
438        Foundation for Strategic Research (SSF). This research used resources of the Advanced  
439        Photon Source, a U.S. Department of Energy (DOE) Office of Science User Facility operated  
440        for the DOE Office of Science by Argonne National Laboratory under Contract No. DE-  
441        AC02-06CH11357. Y.S, P.R, M.M.-M acknowledge the support from the SOLAR ERA NET,  
442        project CUSTCO, number SOL18001. Q.J. aims to acknowledge the Swiss National Science  
443        Foundation (project Nachos: 200021L 172924). V. Tileli and R. Ignatans are gratefully  
444        acknowledged for providing access to the *in-situ* heating TEM holder. The research leading  
445        to these results has received funding from Deutsches Elektronen-Synchrotron DESY and we  
446        would like to thank Arno Jeromin from DESY NanoLab for performing EBSD measurements.

447        **AUTHOR CONTRIBUTIONS**

448        D.D., M.E.S., and M.M.-M. conceived the idea of the project; P.-A.R., Y.S., and M.M.-M.  
449        prepared the samples; D.D., L.A.B.M., G.F., D.S., W.C., R.H., J.W., and M.E.S. performed  
450        the synchrotron experiment; Q.J. performed *in-situ* electron microscopy measurements; D.D.  
451        performed data analysis and prepared the manuscript with contributions from all authors.

452        **COMPETING INTERESTS**

453        The authors declare no competing interests.

## Supplementary Files

This is a list of supplementary files associated with this preprint. Click to download.

- [supplementary.pdf](#)
- [timeInterpolation.avi](#)
- [BrightFieldSTEM.avi](#)